

PAPER

[View Article Online](#)
[View Journal](#)

Cite this: DOI: 10.1039/d0ta00962h

A yolk–shell structured metal–organic framework with encapsulated iron-porphyrin and its derived bimetallic nitrogen-doped porous carbon for an efficient oxygen reduction reaction†

Chaochao Zhang,^{†a} Hao Yang,^{†b} Dan Zhong,^{†c} Yang Xu,^a Yanzhi Wang,^a Qi Yuan,^b Zuozhong Liang,^{ib} Bin Wang,^a Wei Zhang,^{id} Haoquan Zheng,^{id} ^{✉a}
Tao Cheng^{id} ^{✉b} and Rui Cao^{id} ^{✉a}

A yolk–shell structured metal–organic framework (MOF) with encapsulated 5,10,15,20-tetraphenylporphyrinatoiron (FeTPP) in a zeolitic imidazolate framework (ZIF)-L-ZIF-8 is reported. ZIF-L with leaf-like morphology is used as a core, and FeTPP molecules will induce the partial decomposition of ZIF-L. The ZIF-8 shell is formed and encapsulates FeTPP in the yolk–shell structure by adding Zn ions and 2-methylimidazole (Hmim). After pyrolysis, FeCo bimetallic nitrogen doped porous carbon (FeCo–C/N) exhibits ORR performance comparable to commercial Pt/C (20 wt%), with a significant decrease in cost. Density functional theory (DFT) calculations demonstrate that the Fe site in FeCo–C/N contributes to the improved ORR performance by reducing the formation energy of *OOH formation. Thus, a Zn–air battery with FeCo–C/N as an electrocatalyst exhibits significantly improved performance (a high peak power density of 397.25 mW cm^{−2}, and good rechargeable stability). The synthesis strategy presented in this work provides new opportunities for designing yolk–shell structured 2D MOFs for applications in energy conversion and storage.

Received 23rd January 2020
Accepted 26th March 2020

DOI: 10.1039/d0ta00962h

rsc.li/materials-a

Introduction

The sluggish kinetics of the oxygen reduction reaction (ORR) is the bottleneck in the performance of energy conversion and storage devices, such as fuel cells, and metal–air batteries.^{1–4} Precious metal based electrocatalysts have been demonstrated to be among the most efficient and widely used catalysts for the ORR.^{5–13} However, the high cost, the scarcity and the poor stability of the precious metal based ORR electrocatalysts significantly limits the large-scale commercialization of fuel cells, and metal–air batteries.^{14–18} Recently, significant efforts have been made to increase the performance and reduce the cost by developing nonprecious-metal-based catalysts with high activity.^{19–26} Despite the urgent need for low cost catalysis with

comparable (or superior to) the commercial precious metal based catalysts, the experimental synthesis of nonprecious metal based electrocatalysts with high activity and long-term stability are still challenging.

Nitrogen-doped carbon (C/N) materials are considered as potential electrocatalysts due to the different electronegativity between nitrogen and carbon. After introducing a transition metal, the transition metal (M, M = Fe and Co) coordinated NC materials have been developed with enhanced performance in ORR.^{25,27–32} A crucial design of metal–nitrogen coordination site (M–N_x) architectures in M–NC materials is important to determine the overall efficiency and propose the structure–activity relationship. In order to design the M–N_x architectures, one strategy is to use organic molecules as initial ligands, such as porphyrins, corroles and phthalocyanine,^{33–38} that provide four N atoms in a single molecule and could form an M–N_x coordination structure after introducing transition metal ions. To construct composite electrocatalysts, these M–N_x molecules could be immobilized on carbon nanotubes.^{39–42} However, there are still some drawbacks, such as poor charge and mass transfer, low mass efficiency, and poor stability. Another strategy is to construct metal–organic frameworks (MOFs)^{43–46} and covalent organic frameworks (COFs)^{47,48} using M–N_x architecture as linkers or additives. Zeolitic imidazolate frameworks (ZIFs) are a sub-class of MOFs, which have a high N content and are

^aKey Laboratory of Applied Surface and Colloid Chemistry, Ministry of Education, School of Chemistry and Chemical Engineering, Shaanxi Normal University, Xi'an 710119, China. E-mail: zhenghaoquan@snnu.edu.cn; ruicao@ruc.edu.cn

^bInstitute of Functional Nano and Soft Materials (FUNSOM), Jiangsu Key Laboratory for Carbon-Based Functional Materials and Devices, Soochow University, Suzhou 215123, China. E-mail: tcheng@suda.edu.cn

^cZhuhai Da Hengqin Science and Technology Development Co., Ltd, Hengqin New Area, Zhuhai 519000, China

† Electronic supplementary information (ESI) available. See DOI: 10.1039/d0ta00962h

‡ These authors have contributed equally to this work.

proposed as ideal materials for immobilization of M-coordinated porphyrins, corroles or phthalocyanine.^{18,49–63} After pyrolysis at high temperature, M-N_x architectures from parental organic molecules could still be maintained. The NC materials obtained are conductive and porous, which are beneficial for ORR. Recently, two-dimensional (2D) leaf-like ZIF-L has attracted much attention due to its 2D morphology, large surface area, and abundant uncoordinated metal/ligand sites on the outer surface.^{49,64–66} However, after pyrolysis, ZIF-L using Zn as a metal centre would lose its 2D morphology due to the evaporation of Zn which occurred at high temperatures. Therefore, it is difficult to construct a composited catalyst together with a Fe-N_x and control the state of the Fe species without changing the morphology and structure and the synergistic effects of Fe and another transition metal species.⁶⁷

In the research reported herein a yolk-shell structured ZIF was prepared, where 5,10,15,20-tetraphenylporphyrinatoiron (FeTPP) was encapsulated in the void between yolk and shell. The yolk-shell structure could introduce multiple functions to the materials obtained.⁶⁸ The construction of yolk-shell structure in MOFs can normally be achieved by using the hard template method, such as SiO₂, unstable MOF and Cu₂O, or selective acid etching.^{69–73} This work presents a simple strategy to prepare a yolk-shell structured ZIF, where the FeTPP molecules are encapsulated in a yolk-shell ZIF. The ZIF-L using Zn and Co as the metal centre was first prepared as a core, while the FeTPP molecules induced a partial decomposition of ZIF-L. Then, the ZIF-8 shell was initially formed and encapsulated FeTPP in the yolk-shell ZIF. After pyrolysis, the FeCo bimetallic N-doped porous carbons (FeCo-C/N) were obtained. Because of such unique structural and compositional features, FeCo-C/N shows an excellent ORR performance and a good oxygen evolution reaction (OER) performance, which is comparable to that of the commercial Pt/C (20 wt%) and RuO₂, respectively. The FeCo-C/N displays a better electrochemical stability than that of commercial Pt/C. The Zn-air battery using FeCo-C/N as oxygen electrocatalysts exhibits a high performance, and a superior rechargeable stability.

Experimental section

Synthesis of ZIF-L

A portion of Zn(NO₃)₂·6H₂O (0.5 mmol) and 0.5 mmol of Co(NO₃)₂·6H₂O were dissolved in 20 mL of deionized water. 20 mL of aqueous solution containing 8 mmol of Hmim was poured into the aqueous solution of Zn(NO₃)₂·6H₂O and Co(NO₃)₂·6H₂O. After stirring for 4 h, the mixed solution was centrifuged (8000 rpm, 3 min) and washed five times with deionized water. The purple precipitates were dried by freeze drying.

Synthesis of ZIF-L&FeTPP@ZIF-8

The FeTPP was prepared in advance and stored for use (details are described in the Experimental section in the ESI†). Next, 250 mg of ZIF-L was dispersed in 20 mL of methanol and stirred for 10 min, and then 4 mmol of Hmim was added and the

mixture was stirred for 10 min. Then, 5 mg of FeTPP was added and the mixture was stirred for another 10 min. Next, 20 mL of methanol containing 0.5 mmol of Zn(NO₃)₂·6H₂O was added into the methanolic solution of ZIF-L and FeTPP. The solution was stirred for 24 h. The precipitates were centrifuged (10 000 rpm, 5 min) and washed three times with methanol, then the ZIF-L&FeTPP@ZIF-8 was obtained by freeze drying overnight. The ZIF-L@ZIF-8 was synthesized by the same method but without the addition of FeTPP.

Synthesis of FeCo-C/N

A portion of ZIF-L&FeTPP@ZIF-8 (100 mg) was placed in a tube furnace. It was heated to 900 °C and kept for 2 h in flowing N₂ with a flow rate of 5 °C min^{−1}. The black powder obtained was FeCo-C/N. The Co-C/N-1 and Co-C/N-2 were obtained by the same method except that ZIF-L&FeTPP@ZIF-8 were replaced with ZIF-L or ZIF-L@ZIF-8.

Electrochemical evaluation

All the electrochemical measurements were carried out at 30 °C. The ORR performance was tested using a three-electrode system. The working electrode was a rotating disk electrode (RDE) with a diameter of 5 mm (0.196 cm²) or rotating ring disk electrode (RRDE) with a diameter of 5.61 mm (0.247 cm²). The counter electrode was a graphitic rod. The reference electrode was a saturated Ag/AgCl electrode. The cyclic voltammetry (CV) tests used to analyse the ORR were carried out in Ar-saturated or O₂-saturated 0.1 M KOH (scan rate of 100 mV s^{−1}). The linear sweep voltammetry (LSV) tests were carried out in O₂-saturated 0.1 M KOH at rotating speeds ranging from 400 to 1600 rpm (scan rate of 5 mV s^{−1}). The current-time chronoamperometric responses was measured at −0.3 V (*versus* SCE) (sample interval of 0.5 s).

All the OER tests were carried out on a CHI 660E electrochemical workstation at 30 °C. The OER performances were tested using a three-electrode system. The working electrode was a glassy carbon (GC) electrode with a diameter of 3 mm (0.07 cm²) or an indium tin oxide (ITO) electrode with an electrode area of 0.25 cm². The counter electrode was a graphitic rod. The reference electrode was saturated Ag/AgCl electrode. The LSV tests were carried out in 1 M KOH (scan rate of 10 mV s^{−1}). The *j*-*t* measurement was measured at 0.65 V (*versus* SCE; sample interval of 0.5 s).

Zn-air battery evaluation

The anode was prepared using a polished Zn foil (0.25 mm). The electrolyte was a solution with concentrations of 0.2 M ZnCl₂ and 6.0 M KOH, whereas the air electrode was prepared using FeCo-C/N or Pt/C coated carbon cloth (CC)/gas diffusion layer (GDL). A hot-press method was used to attach the CC (1.5 × 1.5 cm²) onto the GDL. A catalyst loading of 2 mg cm^{−2} on the CC/GDL was obtained.

Computational methods

Periodic DFT calculations were performed by using a Vienna *ab initio* simulation package (VASP 5.4.4).⁷⁴ The electron–ion interactions and the interactions between electrons were described by a projector augmented wave (PAW) method and generalized gradient approximation (GGA) with the Perdew–Burke–Ernzerhof (PBE) exchange–correlation functional.⁷⁵ The plane wave basis was expanded to a cutoff energy of 400 eV and the Monkhorst–Pack *k*-point meshes of $3 \times 3 \times 1$. The electron self-consistent calculation was considered to be converged when the energy differences were less than 10^{-5} eV. The structure optimizations were considered to be converged when the force differences were less than $0.02 \text{ eV } \text{\AA}^{-1}$. The semi-empirical dispersion corrected DFT-D3 scheme proposed by Grimme *et al.*⁷⁶ was used to describe the van der Waals (vdW) interactions. The spin polarization effect was taken into consideration. The solvation effect was taken into consideration using the implicit solvation model, VASPsol,⁷⁷ that described the effect of electrostatics, cavitation, and dispersion on the interaction between a solute and solvent as implemented in VASP.

Results and discussion

Characterization of the yolk–shell structured metal–organic framework with encapsulated iron–porphyrin

As shown in Fig. 1, the ZIF-L used as the core was synthesized with $\text{Zn}(\text{NO}_3)_2$, $\text{Co}(\text{NO}_3)_2$ and Hmim. The FeTPP was synthesized in advance and characterized by nuclear magnetic resonance (NMR) and mass spectrometry (MS) (Fig. S1–S3, ESI†). As shown in the scanning electron microscopy (SEM) image, ZIF-L is a leaf-like material with a length of 2–3 μm , a width of 0.5–1 μm , and a thickness of 50 nm (Fig. S4a, ESI†). Next, the solid ZIF-L powders were suspended in methanol. The Hmim, the FeTPP, and the methanolic solution of $\text{Zn}(\text{NO}_3)_2$ were added sequentially. The coating of FeTPP and ZIF-8 did not cause a large change of its morphology and size (Fig. 2a, S4, and S5, ESI†). Interestingly, the transmission electron microscopy (TEM) image and scanning transmission electron microscopy (STEM) image indicated that a yolk–shell structure instead of a core–shell structure was formed (Fig. 2b and S6, ESI†). The elemental EDS mapping was introduced to determine the

location of each species in an individual yolk–shell particle. As shown in Fig. 2c, the Zn and Co elements were located in the yolk and the shell, whereas the Fe element was found mainly in the void between the yolk and the shell. Powder X-ray diffraction (PXRD) patterns indicated the successful formation of ZIF-L, which was the same as in the results of a previous report (Fig. 2d).⁶⁴ The PXRD pattern of ZIF-L&FeTPP@ZIF-8 showed an addition peak at 7.4° , which indicated the formation of ZIF-8. The ZIF-L was a layer-by-layer stacked 2D structure, whereas the ZIF-8 was 3D cubic structure using same building units as ZIF-L (Fig. S7, ESI†). Thus, the FeTPP molecules could be encapsulated in the yolk–shell structure of ZIF-L&FeTPP@ZIF-8. The molecular size of FeTPP was larger than the aperture size of ZIF-8, so the FeTPP cannot escape from the ZIF-8 shell after loading (Fig. S8, ESI†). Unexpectedly, even though no Co source was added during the coating process, the Co element was clearly observed in the shell. Thus, it was important to investigate the formation mechanism of the yolk–shell structure in ZIFs.

The formation mechanism of this yolk–shell structure in the ZIFs was investigated further. The Co element was observed in the shell without adding a Co source, which indicated that the core of the ZIF-L might be partially decomposed during the coating. Control experiments were then carried out. Firstly, ZIF-L particles were suspended in methanol. When a large amount of FeTPP was introduced, the ZIF-L particles collapsed (Fig. S9, ESI†). Thus, FeTPP could induce partial decomposition of the ZIF framework due to the formation of coordination bonds between FeTPP and Hmim in ZIF-L by exchanging the axial ligand of FeTPP.^{78,79} Thus, the concentration of FeTPP on the surface of ZIF-L decreased. This would trigger the diffusion of FeTPP molecules in solution to ZIF-L, whereas the Zn ions, Co ions, and Hmim from the decomposed ZIF-L would diffuse to the outer environment (Fig. 1). When the Zn ions and Co ions diffused out and meet fresh Hmim in solution, a shell of ZIF-8/67 was formed. Finally, the yolk–shell structured ZIF with FeTPP encapsulated was obtained. Compared to the results in previous

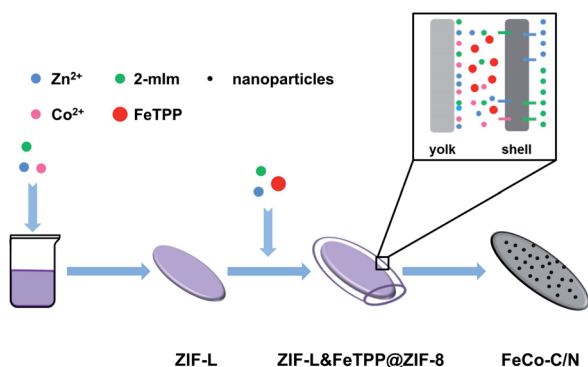


Fig. 1 A schematic illustration of the preparation of FeCo–C/N.

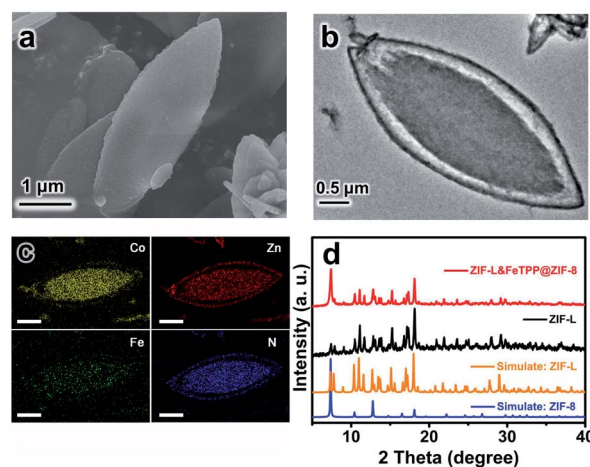


Fig. 2 An SEM image (a), a TEM image (b), and the corresponding EDS mapping (c) of ZIF-L&FeTPP@ZIF-8, and PXRD patterns (d) of ZIF-L&FeTPP@ZIF-8 and ZIF-L. The scale bar in (c) is 1 μm .

work, this unique yolk-shell structure in ZIFs has been successfully prepared using a simple strategy and encapsulated FeTPP in a confined space in the ZIFs, which provides great potential for the preparation of efficient bifunctional electrocatalysts for ORR, OER and a Zn-air battery.

Characterization of yolk-shell structured metal-organic framework derived bimetallic nitrogen-doped porous carbon

After pyrolysis at a high temperature of 900 °C, the material obtained using ZIF-L&FeTPP@ZIF-8 as precursor was denoted as FeCo-C/N. For comparison, the materials prepared by pyrolyzing ZIF-L and ZIF-L&FeTPP@ZIF-8 without FeTPP were denoted as Co-C/N-1 and Co-C/N-2, respectively (Fig. S10, ESI†). The FeCo-C/N remained the primary morphology and showed no change in size (Fig. 3a). In the present work, without further acid treatment, the TEM image of FeCo-C/N shows that the nanoparticles were of 5–20 nm in size in FeCo-C/N and had a homogenous particle size distribution (Fig. 3b). The high-resolution TEM (HRTEM) image shows a lattice fringe with an interplanar spacing of 0.207 nm.⁷ In

addition, these nanoparticles were surrounded by graphitic carbon layers (Fig. 3c). The results of element mapping proved the existence of Fe, Co, and N elements, which were uniformly distributed throughout a FeCo-NC particle (Fig. 3d). The PXRD patterns of FeCo-C/N, Co-C/N-1, and Co-C/N-2 indicate the formation of face-centered-cubic (fcc) Co nanocrystals (β -Co JCPDS 15-0806) (Fig. 3e). The diffraction peak at 44.2° corresponded to the plane (111) of β -Co, which was consistent with the results of the HRTEM. The Raman spectra of FeCo-C/N, Co-C/N-1, and Co-C/N-2 show two obvious peaks, one is the D band at 1350 cm⁻¹ and the other is the G band at 1580 cm⁻¹, which were attributed to disordered carbon and graphitic carbon, respectively (Fig. 3f). The intensity ratio of I_D to I_G is a parameter used to determine the amount of defective carbon in materials. The values of I_D to I_G of FeCo-C/N, Co-C/N-1, and Co-C/N-2 were 0.9, 0.65, and 0.85, respectively. The FeCo-C/N had more defects due to the construction of the yolk-shell structure in the ZIFs. The Brunauer-Emmett-Teller (BET) surface area of FeCo-C/N was 347.7 m² g⁻¹, which was larger than those of Co-C/N-1 (300.9 m² g⁻¹) and Co-C/N-2 (306.2 m² g⁻¹) (Fig. S11, ESI†).

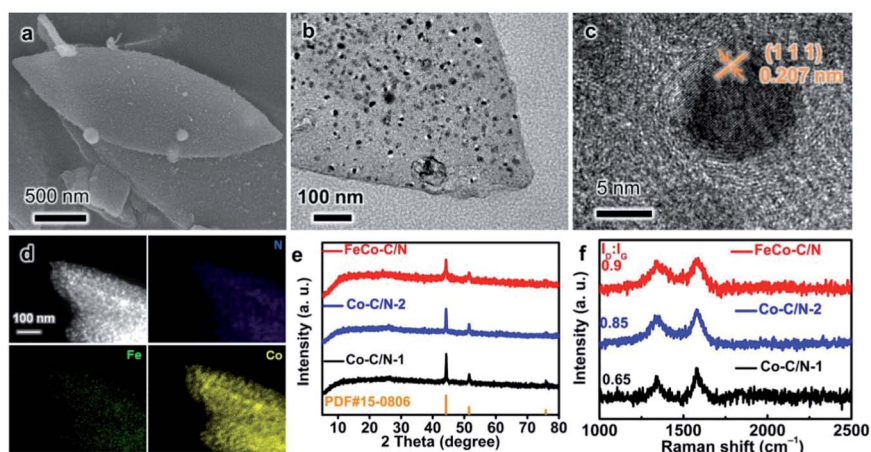


Fig. 3 An SEM image (a), a TEM image (b), a HRTEM image (c), and the corresponding EDS mapping (d) of FeCo-C/N, and the PXRD patterns (e) and the Raman spectra (f) of the electrocatalysts.

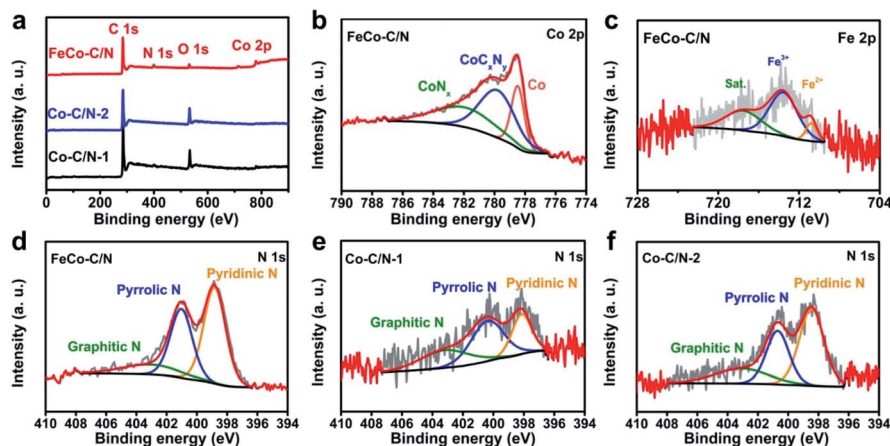


Fig. 4 (a) XPS spectra of FeCo-C/N, Co-C/N-1 and Co-C/N-2. High-resolution XPS spectra of (b) Co 2p and (c) Fe 2p for FeCo-C/N. High-resolution XPS spectra of N 1s for FeCo-C/N (d), Co-C/N-1 (e), and Co-C/N-2 (f).

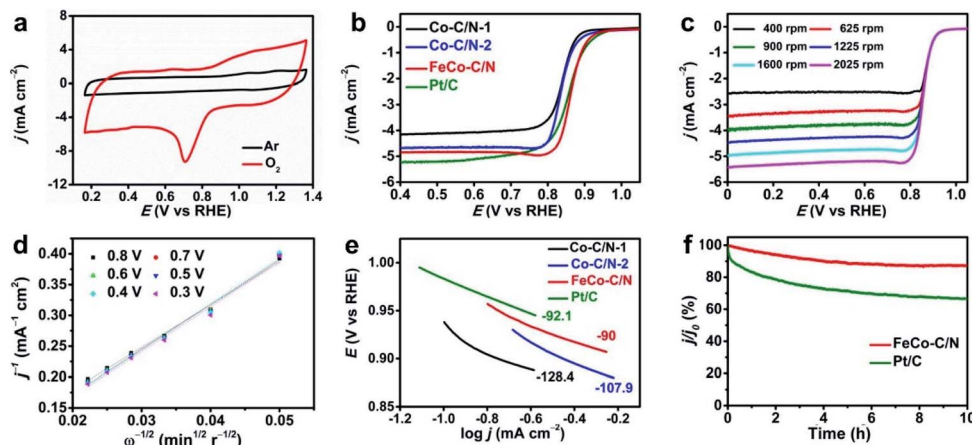


Fig. 5 (a) CVs from FeCo-C/N in Ar-saturated and O₂-saturated 0.1 M KOH aqueous solution. (b) The LSV curves of different catalysts in O₂-saturated 0.1 M KOH at 1600 rpm. (c) LSV curves of FeCo-C/N at various rotational speeds and (d) K-L plots of FeCo-C/N at different potentials. (e) Tafel slopes of different catalysts. (f) Current-time (*j*-*t*) profiles for Pt/C and FeCo-C/N at 0.664 V (versus RHE).

The results of the X-ray photoelectron spectroscopy (XPS) demonstrated the existence of Fe, Co, N, C (Fig. 4). Three types of Co species, metallic Co (778.4 eV), CoC_xN_y (779.8 eV), and CoN_x (781.9 eV), were observed (Fig. 4b, and S12, ESI†). As shown in Fe 2p for FeCo-C/N, the peaks at 713.1 eV and 710.9 eV contributed to the Fe(III) species and Fe(II) species, respectively, suggesting that Fe existed as the Fe(III) species and Fe(II) in the possible form of Fe-N_x (Fig. 4c).^{82,83} The peak at 708 eV attributed to metallic Fe was not observed in the high-resolution XPS spectra, indicating that the FeCo alloy was not formed in FeCo-C/N. This observation was different from that found in previous reports. The FeCo alloy nanoparticles were formed normally after pyrolysis of FeCo metallic MOFs, when Fe and Co were homogeneously distributed in the MOFs.^{82,83} In the yolk-shell structured ZIFs, the FeTPP molecules were located in a confined space between the core and the shell, which maintained a partial Fe-N_x structure during pyrolysis. Furthermore, the XPS peaks assigned to Fe₃O₄ were not observed. The absence of FeO_x nanoparticles in FeCo-C/N was also confirmed by its EDS pattern. No diffraction rings assigned to FeO_x were observed. The contents of three N species, pyridinic N (398.8 eV), pyrrolic N (401.0 eV), graphitic N (403.0 eV) are summarized in Fig. 4d-f and Table S1 (ESI†). The FeCo-C/N possessed the highest content of pyridinic N and the lowest graphitic N. This result indicated that there are more defects in FeCo-C/N, which was consistent with the results of the Raman spectroscopy. As previously reported, the construction of a heterogeneous interface in MOFs could induce the formation of a defective layered structure, when two different species move to the same interface during pyrolysis. Therefore, all these features were beneficial to the enhanced ORR performance.

Electrochemical studies of bimetallic nitrogen-doped porous carbon for the oxygen reduction reaction

To compare the ORR performances of the catalysts, a series of electrochemical tests were carried out. As shown in the CV curves, FeCo-C/N had an immediately reductive peak in O₂

saturated solution, indicating its ORR activity (Fig. 5a). As shown in the LSV curves, the FeCo-C/N showed a more positive half-wave potential (0.864 V) than those of Co-C/N-1 (0.83 V), Co-C/N-2 (0.836 V) and other reported electrocatalysts (Table S3†), which was also comparable to that of the Pt/C (0.86 V) (Fig. 5b). To calculate the transfer numbers (*n*), LSVs with different rotational speeds and Koutecky-Levich (K-L) plots of FeCo-C/N were tested (Fig. 5c and d). The electron transfer number (*n*) of the FeCo-C/N was about 3.88, which was close to the value obtained using the RRDE (Fig. S13, and Table S2, ESI†). The Tafel slope of FeCo-C/N was 90 mV dec⁻¹, which was smaller than those of Co-C/N-1 (128.4 mV dec⁻¹), Co-C/N-2

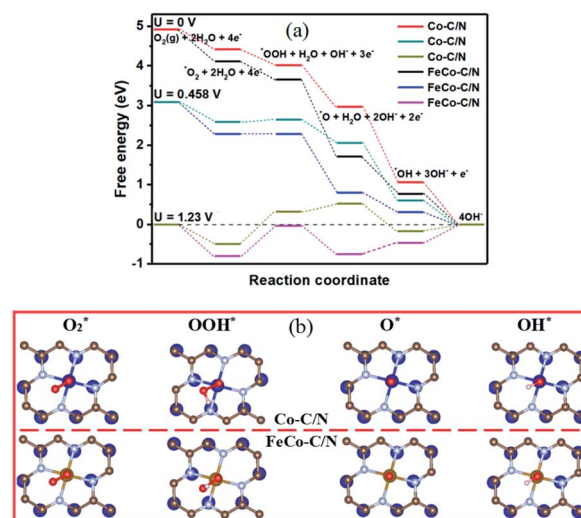
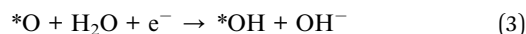
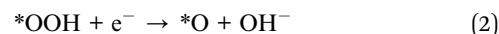


Fig. 6 (a) The free energy diagrams of the oxygen reduction reaction (ORR) pathway on FeCo-C/N (in black) and Co-C/N (in red) at electrode potentials of 0 V, 0.458 V and 1.23 V. *OOH formation was noted as the potential determining step in both cases. (b) The optimized atomic structures of *O₂, *OOH, *O and *OH on Co-C/N and FeCo-C/N. The colors are Co in blue, Fe in yellow, C in brown, N in cyan, and H in white.

(107.9 mV dec⁻¹) and Pt/C (92.1 mV dec⁻¹) (Fig. 5e). The consequence of the *j*-*t* chronoamperometric responses is shown in Fig. 5f. The FeCo-C/N possessed better stability than the Pt/C catalyst. After 10 h, the current density of the FeCo-C/N decreased less than 10%. Therefore, the FeCo-C/N electrocatalyst displayed a high ORR activity and a better stability than that of commercial Pt/C.

The DFT calculations were carried out to investigate the reaction pathway of ORR on Co-C/N and FeCo-C/N on the level of the PBE plane wave with a D3 vdW correction. The simulation models consisted of four layers of a 4 × 4 Co (111) surface with one adsorbed N-doped graphene monolayer on it. The in-plane cell parameters between the Co (111) surface and the N-doped graphene were close: 2.51 Å for Co and 2.46 Å for N-doped graphene, which takes into account an ignorable lattice mismatch within 1%. The single atom metal site of Co-C/N was Co, and the single atom metal site of FeCo-C/N was Fe. It was considered that these simulation models represented the experiment well and at the same time kept the balance of accuracy and efficiency. More details about the simulation models are given in the ESI. Four reactive intermediates (*O₂, *OOH, *O and *OH) were considered in the calculations and the optimized atomic structures are shown in Fig. 6.

Despite the existence of diverse opinions, one of the mostly accepted ORR reaction mechanisms is as follows:⁸⁴



The free energy differences (ΔG) of these four elementary reactions are shown in Fig. 6, Tables S4 and S5 (ESI†). For Co-C/N, the *OOH formation had the highest ΔG of -0.406 eV, which indicated that the *OOH formation was the potential determining step (PDS) of ORR on Co-C/N, and the overpotential (η) was 0.824 V. For FeCo-C/N, *OOH formation was also the PDS, which had the highest ΔG of -0.458 eV, and the η was 0.772 V. Thus, it was predicted that introducing Fe leads to a 0.052 eV decrease in ΔG , which indicated that the improved ORR performance was due to the reduced formation energy of *OOH by introducing the Fe, instead of changing the reaction mechanism. These predictions agreed well with the experimental observations.

Electrochemical studies of bimetallic nitrogen-doped porous carbon for the oxygen evolution reaction

To investigate the OER performances of the catalysts, a series of tests were carried out. As shown from the LSV curves in 1 M KOH (Fig. 7a), FeCo-C/N exhibited a lower overpotential of

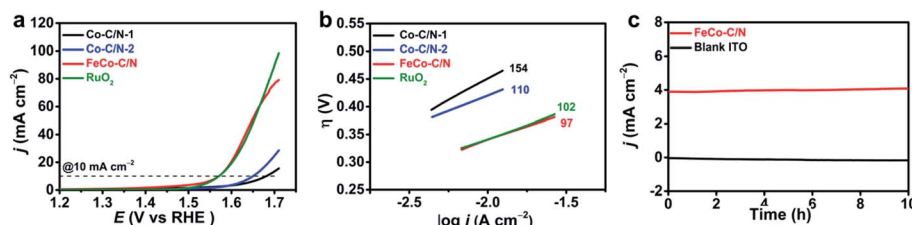


Fig. 7 (a) LSV curves and (b) Tafel plots of different catalysts in 1.0 M KOH. (c) *j*-*t* measurements for the FeCo-C/N catalyst at 0.65 V (vs. SCE) in 1.0 M KOH.

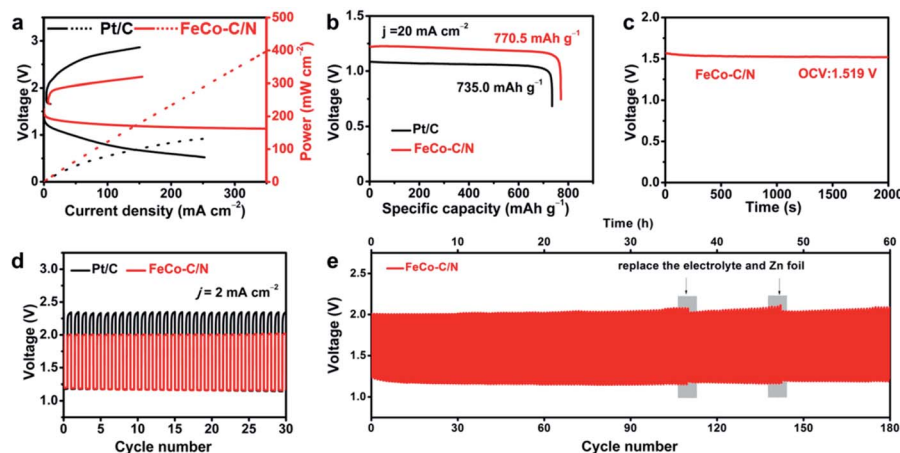


Fig. 8 Charge and discharge polarization curves (a), discharge curves at 20 mA cm⁻² (b), open circuit plots (c), galvanostatic discharge-charge cycling curves at 2 mA cm⁻² (d), and the long-time cycling of a rechargeable Zn-air battery using FeCo-C/N and Pt/C at 2 mA cm⁻² (e).

353 mV at 10 mA cm⁻² than those of Co-C/N-1 (473 mV at 10 mA cm⁻²) and Co-C/N-2 (432 mV at 10 mA cm⁻²), which was also comparable to that of RuO₂ (335 mV at 10 mA cm⁻²). The Tafel slope of FeCo-C/N was measured as 102 mV dec⁻¹, which was much smaller than those of Co-C/N-1 (154 mV dec⁻¹) and Co-C/N-2 (110 mV dec⁻¹) (Fig. 7b). The *j*-*t* measurements of the FeCo-C/N catalyst, further indicated that the FeCo-C/N catalyst possessed a good OER activity after 10 h of testing in an alkaline solution (Fig. 7c).

Zn-air battery assembled using bimetallic nitrogen-doped porous carbon

To further evaluate the properties of the FeCo-C/N catalyst, a Zn-air battery was assembled.^{85,86} Clean Zn foil was used as the anode, whereas FeCo-C/N catalyst loading on carbon cloth was used as the cathode. The electrolyte was a mixed solution of 0.2 M ZnCl₂ and 6 M KOH. As shown in Fig. 8a, the FeCo-C/N catalyst had a higher discharge current than the Pt/C. In addition, the FeCo-C/N catalyst had a lower charging voltage and a higher discharging voltage, which gave a better charge-discharge performance than the Pt/C catalyst. The power density of the FeCo-C/N catalyst was 397.25 mW cm⁻², which was one of the best results out of all the reported electrocatalysts and was triple that of Pt/C (131.54 mW cm⁻²) (Table S6, ESI†). The specific capacity was calculated to be 770.5 mA h g⁻¹ at a current density of 20 mA cm⁻², which was higher than that of Pt/C (735.0 mA h g⁻¹) (Fig. 8b). As shown in Fig. 8c, the FeCo-C/N catalyst showed a stable open-circuit voltage (OCV) of 1.519 V. The battery using FeCo-C/N exhibited a good cyclic stability with an initial charging potential of 2.0 V and a discharging potential of 1.2 V (Fig. 8d). As shown in Fig. 8e, the Zn-air battery using FeCo-C/N catalyst displayed a very stable performance in a long term test (60 h).

Conclusions

In conclusion, a straightforward strategy was developed to encapsulate FeTPP into the confined space of ZIFs with a yolk-shell structure. After pyrolysis, the obtained FeCo-C/N retains a 2D morphology, high surface area, more defects and more exposed active sites, which are all beneficial for the ORR. FeCo-C/N displayed a high ORR activity with a half-wave potential of 0.864 V and OER activity with a low overpotential of 353 mV at 10 mA cm⁻². A constructed Zn-air battery using FeCo-C/N electrocatalysts also shows a peak power density as high as 397.25 mW cm⁻² (three times higher than that of Pt/C), and good rechargeable stability. This work provides opportunities for the design of composite materials of M-N_x molecules and yolk-shell structured MOFs for energy related applications.

Conflicts of interest

There are no conflicts to declare.

Acknowledgements

This work was supported by the National Natural Science Foundation of China (Grant No. 21975148, 2190030094, 21601118, 21773146, and 21808138), the Fundamental Research Funds for the Central Universities, the Natural Science Foundation of Jiangsu Province (Grant No. SBK20190810), the Jiangsu Province High-Level Talents (JNHB-106), the Research Funds of Shaanxi Normal University (GK201903033), Fok Ying-Tong Education Foundation for Outstanding Young Teachers in University, and the China Postdoctoral Science Foundation (No. 2019T120877, and 2019M660128). TC and HY are supported by grants from the startup supports of Soochow University and TC is also supported by the Program for Jiangsu Specially-Appointed Professors. We acknowledge Shanghai Supercomputer Center for providing the computational resources for this work. This work was partly supported by the Collaborative Innovation Center of Suzhou Nano Science & Technology, the Priority Academic Program Development of Jiangsu Higher Education Institutions (PAPD), and the 111 Project.

Notes and references

- 1 Z. W. Seh, J. Kibsgaard, C. F. Dickens, I. Chorkendorff, J. K. Nørskov and T. F. Jaramillo, *Science*, 2017, **355**, eaad4998.
- 2 J. Li, H.-M. Yin, X.-B. Li, E. Okunishi, Y.-L. Shen, J. He, Z.-K. Tang, W.-X. Wang, E. Yücelen, C. Li, Y. Gong, L. Gu, S. Miao, L.-M. Liu, J. Luo and Y. Ding, *Nat. Energy*, 2017, **2**, 17111.
- 3 W. Zhang, W. Lai and R. Cao, *Chem. Rev.*, 2017, **117**, 3717–3797.
- 4 Z. Chen, D. Higgins, A. Yu, L. Zhang and J. Zhang, *Energy Environ. Sci.*, 2011, **4**, 3167–3192.
- 5 R. Balgis, W. Widiyastuti, T. Ogi and K. Okuyama, *ACS Appl. Mater. Interfaces*, 2017, **9**, 23792–23799.
- 6 Y. Guo, P. Yuan, J. Zhang, H. Xia, F. Cheng, M. Zhou, J. Li, Y. Qiao, S. Mu and Q. Xu, *Adv. Funct. Mater.*, 2018, **28**, 1805641.
- 7 H. Zhu, Y. Cai, F. Wang, P. Gao and J. Cao, *ACS Appl. Mater. Interfaces*, 2018, **10**, 22156–22166.
- 8 Z. Zhao, C. Chen, Z. Liu, J. Huang, M. Wu, H. Liu, Y. Li and Y. Huang, *Adv. Mater.*, 2019, **31**, 1808115.
- 9 W.-J. Jiang, L. Gu, L. Li, Y. Zhang, X. Zhang, L.-J. Zhang, J.-Q. Wang, J.-S. Hu, Z. Wei and L.-J. Wan, *J. Am. Chem. Soc.*, 2016, **138**, 3570–3578.
- 10 L. Lai, J. R. Potts, D. Zhan, L. Wang, C. K. Poh, C. Tang, H. Gong, Z. Shen, J. Lin and R. S. Ruoff, *Energy Environ. Sci.*, 2012, **5**, 7936–7942.
- 11 X. Tian, X. Zhao, Y.-Q. Su, L. Wang, H. Wang, D. Dang, B. Chi, H. Liu, E. J. M. Hensen, X. W. Lou and B. Y. Xia, *Science*, 2019, **366**, 850.
- 12 L. Bu, N. Zhang, S. Guo, X. Zhang, J. Li, J. Yao, T. Wu, G. Lu, J.-Y. Ma, D. Su and X. Huang, *Science*, 2016, **354**, 1410.
- 13 Z. Liang, X. Fan, H. Lei, J. Qi, Y. Li, J. Gao, M. Huo, H. Yuan, W. Zhang, H. Lin, H. Zheng and R. Cao, *Angew. Chem., Int. Ed.*, 2018, **57**, 13187–13191.

- 14 Z.-L. Wang, D. Xu, J.-J. Xu and X.-B. Zhang, *Chem. Soc. Rev.*, 2014, **43**, 7746–7786.
- 15 C.-Y. Su, H. Cheng, W. Li, Z.-Q. Liu, N. Li, Z. Hou, F.-Q. Bai, H.-X. Zhang and T.-Y. Ma, *Adv. Energy Mater.*, 2017, **7**, 1602420.
- 16 Y. Li, M. Gong, Y. Liang, J. Feng, J.-E. Kim, H. Wang, G. Hong, B. Zhang and H. Dai, *Nat. Commun.*, 2013, **4**, 1805.
- 17 X. Wan, X. Liu, Y. Li, R. Yu, L. Zheng, W. Yan, H. Wang, M. Xu and J. Shui, *Nat. Catal.*, 2019, **2**, 259–268.
- 18 W. Xia, J. Tang, J. Li, S. Zhang, K. C. W. Wu, J. He and Y. Yamauchi, *Angew. Chem., Int. Ed.*, 2019, **58**, 13354–13359.
- 19 K. Holst-Olesen, L. Silvili, J. Rossmeisl and M. Arenz, *ACS Catal.*, 2019, **9**, 3082–3089.
- 20 X. Huang, T. Shen, T. Zhang, H. Qiu, X. Gu, Z. Ali and Y. Hou, *Adv. Energy Mater.*, 2019, **9**, 1900375.
- 21 Y. Sha, T. H. Yu, B. V. Merinov and W. A. Goddard, *ACS Catal.*, 2014, **4**, 1189–1197.
- 22 D. Singh, K. Mamtani, C. R. Bruening, J. T. Miller and U. S. Ozkan, *ACS Catal.*, 2014, **4**, 3454–3462.
- 23 C. Du, P. Li, F. Yang, G. Cheng, S. Chen and W. Luo, *ACS Appl. Mater. Interfaces*, 2018, **10**, 753–761.
- 24 A. A. Gewirth, J. A. Varnell and A. M. DiAscro, *Chem. Rev.*, 2018, **118**, 2313–2339.
- 25 Z. Liang, C. Zhang, H. Yuan, W. Zhang, H. Zheng and R. Cao, *Chem. Commun.*, 2018, **54**, 7519–7522.
- 26 L. Xie, X. Li, B. Wang, J. Meng, H. Lei, W. Zhang and R. Cao, *Angew. Chem., Int. Ed.*, 2019, **58**, 18883–18887.
- 27 W. J. Jiang, L. Gu, L. Li, Y. Zhang, X. Zhang, L. J. Zhang, J. Q. Wang, J. S. Hu, Z. Wei and L. J. Wan, *J. Am. Chem. Soc.*, 2016, **138**, 3570–3578.
- 28 D. Saliba, M. Ammar, M. Rammal, M. Al-Ghoul and M. Hmadeh, *J. Am. Chem. Soc.*, 2018, **140**, 1812–1823.
- 29 R. Jasinski, *Nature*, 1964, **201**, 1212–1213.
- 30 W. Wang, Q. Jia, S. Mukerjee and S. Chen, *ACS Catal.*, 2019, **9**, 10126–10141.
- 31 C. Zhu, H. Li, S. Fu, D. Du and Y. Lin, *Chem. Soc. Rev.*, 2016, **45**, 517–531.
- 32 W. He, Y. Wang, C. Jiang and L. Lu, *Chem. Soc. Rev.*, 2016, **45**, 2396–2409.
- 33 Y. Jiang, Y. Lu, X. Lv, D. Han, Q. Zhang, L. Niu and W. Chen, *ACS Catal.*, 2013, **3**, 1263–1271.
- 34 S. Yasuda, A. Furuya, Y. Uchibori, J. Kim and K. Murakoshi, *Adv. Funct. Mater.*, 2016, **26**, 738–744.
- 35 P. M. Usov, B. Huffman, C. C. Epley, M. C. Kessinger, J. Zhu, W. A. Maza and A. J. Morris, *ACS Appl. Mater. Interfaces*, 2017, **9**, 33539–33543.
- 36 R. Jiang, L. Li, T. Sheng, G. Hu, Y. Chen and L. Wang, *J. Am. Chem. Soc.*, 2018, **140**, 11594–11598.
- 37 Y. Wang, M. Wang, Z. Zhang, Q. Wang, Z. Jiang, M. Lucero, X. Zhang, X. Li, M. Gu, Z. Feng and Y. Liang, *ACS Catal.*, 2019, **9**, 6252–6261.
- 38 N. Wang, H. Lei, Z. Zhang, J. Li, W. Zhang and R. Cao, *Chem. Sci.*, 2019, **10**, 2308–2314.
- 39 Y. Wu, Z. Jiang, X. Lu, Y. Liang and H. Wang, *Nature*, 2019, **575**, 639–642.
- 40 X. Li, H. Lei, J. Liu, X. Zhao, S. Ding, Z. Zhang, X. Tao, W. Zhang, W. Wang, X. Zheng and R. Cao, *Angew. Chem., Int. Ed.*, 2018, **57**, 15070–15075.
- 41 H. Lei, C. Liu, Z. Wang, Z. Zhang, M. Zhang, X. Chang, W. Zhang and R. Cao, *ACS Catal.*, 2016, **6**, 6429–6437.
- 42 J. Meng, H. Lei, X. Li, J. Qi, W. Zhang and R. Cao, *ACS Catal.*, 2019, **9**, 4551–4560.
- 43 D. Feng, Z. Y. Gu, J. R. Li, H. L. Jiang, Z. Wei and H. C. Zhou, *Angew. Chem., Int. Ed.*, 2012, **51**, 10307–10310.
- 44 Y. Bai, Y. Dou, L.-H. Xie, W. Rutledge, J.-R. Li and H.-C. Zhou, *Chem. Soc. Rev.*, 2016, **45**, 2327–2367.
- 45 M. Zhao, Y. Wang, Q. Ma, Y. Huang, X. Zhang, J. Ping, Z. Zhang, Q. Lu, Y. Yu, H. Xu, Y. Zhao and H. Zhang, *Adv. Mater.*, 2015, **27**, 7372–7378.
- 46 S. Lin, C. S. Diercks, Y.-B. Zhang, N. Kornienko, E. M. Nichols, Y. Zhao, A. R. Paris, D. Kim, P. Yang, O. M. Yaghi and C. J. Chang, *Science*, 2015, **349**, 1208.
- 47 B.-Q. Li, S.-Y. Zhang, B. Wang, Z.-J. Xia, C. Tang and Q. Zhang, *Energy Environ. Sci.*, 2018, **11**, 1723–1729.
- 48 B.-Q. Li, S.-Y. Zhang, L. Kong, H.-J. Peng and Q. Zhang, *Adv. Mater.*, 2018, **30**, 1707483.
- 49 R. Chen, J. Yao, Q. Gu, S. Smeets, C. Baerlocher, H. Gu, D. Zhu, W. Morris, O. M. Yaghi and H. Wang, *Chem. Commun.*, 2013, **49**, 9500–9502.
- 50 J. Tang, R. R. Salunkhe, J. Liu, N. L. Torad, M. Imura, S. Furukawa and Y. Yamauchi, *J. Am. Chem. Soc.*, 2015, **137**, 1572–1580.
- 51 H. Tabassum, W. Guo, W. Meng, A. Mahmood, R. Zhao, Q. Wang and R. Zou, *Adv. Energy Mater.*, 2017, **7**, 1601671.
- 52 Y.-Z. Chen, C. Wang, Z.-Y. Wu, Y. Xiong, Q. Xu, S.-H. Yu and H.-L. Jiang, *Adv. Mater.*, 2015, **27**, 5010–5016.
- 53 H.-L. Jiang, B. Liu, Y.-Q. Lan, K. Kuratani, T. Akita, H. Shioyama, F. Zong and Q. Xu, *J. Am. Chem. Soc.*, 2011, **133**, 11854–11857.
- 54 S. Zheng, X. Li, B. Yan, Q. Hu, Y. Xu, X. Xiao, H. Xue and H. Pang, *Adv. Energy Mater.*, 2017, **7**, 1602733.
- 55 S. Liu, Z. Wang, S. Zhou, F. Yu, M. Yu, C.-Y. Chiang, W. Zhou, J. Zhao and J. Qiu, *Adv. Mater.*, 2017, **29**, 1700874.
- 56 H. Zheng, Y. Zhang, L. Liu, W. Wan, P. Guo, A. M. Nyström and X. Zou, *J. Am. Chem. Soc.*, 2016, **138**, 962–968.
- 57 L. Shang, H. Yu, X. Huang, T. Bian, R. Shi, Y. Zhao, G. I. N. Waterhouse, L.-Z. Wu, C.-H. Tung and T. Zhang, *Adv. Mater.*, 2016, **28**, 1668–1674.
- 58 M. Kuang, Q. Wang, P. Han and G. Zheng, *Adv. Energy Mater.*, 2017, **7**, 1700193.
- 59 Y. Li, B. Jia, Y. Fan, K. Zhu, G. Li and C.-Y. Su, *Adv. Energy Mater.*, 2018, **8**, 1702048.
- 60 L. Jiao and H.-L. Jiang, *Chem*, 2019, **5**, 786–804.
- 61 J. Meng, C. Niu, L. Xu, J. Li, X. Liu, X. Wang, Y. Wu, X. Xu, W. Chen, Q. Li, Z. Zhu, D. Zhao and L. Mai, *J. Am. Chem. Soc.*, 2017, **139**, 8212–8221.
- 62 B. Y. Xia, Y. Yan, N. Li, H. B. Wu, X. W. Lou and X. Wang, *Nat. Energy*, 2016, **1**, 15006.
- 63 B. Wang, A. P. Côté, H. Furukawa, M. O’Keeffe and O. M. Yaghi, *Nature*, 2008, **453**, 207–211.

- 64 T. Wang, Z. Kou, S. Mu, J. Liu, D. He, I. S. Amiinu, W. Meng, K. Zhou, Z. Luo, S. Chaemchuen and F. Verpoort, *Adv. Funct. Mater.*, 2018, **28**, 1705048.
- 65 J. Guan, Y. Hu, Y. Wang, H. Li, Z. Xu, T. Zhang, P. Wu, S. Zhang, G. Xiao, W. Ji, L. Li, M. Zhang, Y. Fan, L. Li, B. Zheng, W. Zhang, W. Huang and F. Huo, *Adv. Mater.*, 2017, **29**, 1606290.
- 66 Y. Zhou, Y. Xu, C. Zhang, Å. Emmer and H. Zheng, *Anal. Chem.*, 2020, **92**, 2151–2158.
- 67 Y. Pan, K. Sun, S. Liu, X. Cao, K. Wu, W. C. Cheong, Z. Chen, Y. Wang, Y. Li, Y. Liu, D. Wang, Q. Peng, C. Chen and Y. Li, *J. Am. Chem. Soc.*, 2018, **140**, 2610–2618.
- 68 Y. Yang, X. Liu, X. Li, J. Zhao, S. Bai, J. Liu and Q. Yang, *Angew. Chem., Int. Ed.*, 2012, **51**, 9164–9168.
- 69 K.-K. Sun, S.-J. Chen, Z.-L. Li, G.-P. Lu and C. Cai, *Green Chem.*, 2019, **21**, 1602–1608.
- 70 X.-Y. Liu, F. Zhang, T.-W. Goh, Y. Li, Y.-C. Shao, L. Luo, W. Huang, Y.-T. Long, L.-Y. Chou and C.-K. Tsung, *Angew. Chem., Int. Ed.*, 2018, **57**, 2110–2114.
- 71 C.-H. Kuo, Y. Tang, L.-Y. Chou, B. T. Sneed, C. N. Brodsky, Z. Zhao and C.-K. Tsung, *J. Am. Chem. Soc.*, 2012, **134**, 14345–14348.
- 72 L. Luo, W.-S. Lo, X. Si, H. Li, Y. Wu, Y. An, Q. Zhu, L.-Y. Chou, T. Li and C.-K. Tsung, *J. Am. Chem. Soc.*, 2019, **141**, 20365–20370.
- 73 P. Zhang, B. Y. Guan, L. Yu and X. W. Lou, *Chem*, 2018, **4**, 162–173.
- 74 G. Kresse and J. Furthmüller, *Phys. Rev. B: Condens. Matter Mater. Phys.*, 1996, **54**, 11169–11186.
- 75 J. P. Perdew, K. Burke and M. Ernzerhof, *Phys. Rev. Lett.*, 1996, **77**, 3865–3868.
- 76 S. Grimme, J. Antony, S. Ehrlich and H. Krieg, *J. Chem. Phys.*, 2010, **132**, 154104.
- 77 K. Mathew, R. Sundararaman, K. Letchworth-Weaver, T. A. Arias and R. G. Hennig, *J. Chem. Phys.*, 2014, **140**, 084106.
- 78 X. Tian, C. Lin, Z. Zhong, X. Li, X. Xu, J. Liu, L. Kang, G. Chai and J. Yao, *Cryst. Growth Des.*, 2019, **19**, 3279–3287.
- 79 H. Lei, X. Li, J. Meng, H. Zheng, W. Zhang and R. Cao, *ACS Catal.*, 2019, **9**, 4320–4344.
- 80 M. Zhang, Q. Dai, H. Zheng, M. Chen and L. Dai, *Adv. Mater.*, 2018, **30**, 1705431.
- 81 Z. Li, M. Shao, L. Zhou, R. Zhang, C. Zhang, M. Wei, D. G. Evans and X. Duan, *Adv. Mater.*, 2016, **28**, 2337–2344.
- 82 N. R. Sahraie, U. I. Kramm, J. Steinberg, Y. Zhang, A. Thomas, T. Reier, J.-P. Paraknowitsch and P. Strasser, *Nat. Commun.*, 2015, **6**, 8618.
- 83 Z. Wang, H. Jin, T. Meng, K. Liao, W. Meng, J. Yang, D. He, Y. Xiong and S. Mu, *Adv. Funct. Mater.*, 2018, **28**, 1802596.
- 84 L. Zhang and Z. Xia, *J. Phys. Chem. C*, 2011, **115**, 11170–11176.
- 85 J. Liu, T. He, Q. Wang, Z. Zhou, Y. Zhang, H. Wu, Q. Li, J. Zheng, Z. Sun, Y. Lei, J. Ma and Y. Zhang, *J. Mater. Chem. A*, 2019, **7**, 12451–12456.
- 86 M. Tan, T. He, J. Liu, H. Wu, Q. Li, J. Zheng, Y. Wang, Z. Sun, S. Wang and Y. Zhang, *J. Mater. Chem. A*, 2018, **6**, 8227–8232.